Q. J. R. Meteorol. Soc. (2005), **131**, pp. 2539–2557 doi: 10.1256/qj.04.150

Temperature and salinity dependence of sea surface emissivity in the thermal infrared

By S. M. NEWMAN*, J. A. SMITH, M. D. GLEW, S. M. ROGERS and J. P. TAYLOR
Met Office, Exeter, UK

(Received 15 October 2004; revised 25 May 2005)

SUMMARY

Aircraft and ground-based interferometer measurements are used to investigate the dependence of sea surface emissivity on water temperature and salinity in the infrared spectral region. The effect of dissolved salts is found to be small and in line with previous studies, whereas temperature (often neglected in current emissivity models) has a greater impact. The influence on satellite sea surface temperature (SST) retrievals is found to be significant for high-resolution infrared sounders: neglecting a temperature-dependent emissivity leads to systematic errors in SST of as much as 0.6 K depending on channel frequency.

KEYWORDS: Infrared remote sensing Sea surface temperature

1. INTRODUCTION

The ability to measure sea surface temperatures (SSTs) accurately from space is essential both for data assimilation into weather forecasting models and monitoring long term climate trends. Water is a non-black-body emitter with an emissivity slightly less than one, so the spectral variation of the emissivity must be known in order to infer SSTs from measurements of infrared radiance. Numerical computations of emissivity parametrized for view angle and surface roughness (see e.g. Masuda *et al.* 1988) have been used extensively in satellite retrieval algorithms. It is estimated that satellite SST products must be accurate to within 0.3 K (Smith *et al.* 1996 and references therein) for useful climate research. The next generation of high-resolution infrared sounders (AIRS, Aumann and Miller 1995; IASI, Cayla and Javelle 1995) will, therefore, require the emission characteristics of the ocean surface to be well characterized.

Previous validation studies (Fiedler and Bakan 1997; Wu and Smith 1997; Minnett *et al.* 2001) found broad agreement of measured emissivity with theoretical values, though with some unexplained features around 830–900 cm^{-1}. Previously (Taylor *et al.* 2003) noted discrepancies in the modelling of aircraft radiance observations from flights over the Baltic Sea, and postulated a possible temperature or salinity dependence of the emissivity to account for this. Here we extend the analysis of aircraft measurements over contrasting ocean conditions, and pursue complementary ground-based studies with a standardized water surface. In this way we quantify the effects of salinity and temperature on sea surface emissivity, and estimate the impact on satellite SST retrievals of neglecting these factors.

2. EMISSIVITY RETRIEVAL METHOD

In general the reflectance of a flat water surface is governed by Fresnel's equations (see Wu and Smith (1997) for a detailed discussion). Given that the transmissivity of water in the infrared is small, the flat surface emissivity is simply:

$$\varepsilon(\mathbf{n}, \chi) = 1 - \rho(\mathbf{n}, \chi), \tag{1}$$

* Corresponding author: Met Office, Cordouan 2, FitzRoy Road, Exeter, Devon EX1 3PB, UK.
e-mail: stu.newman@metoffice.gov.uk

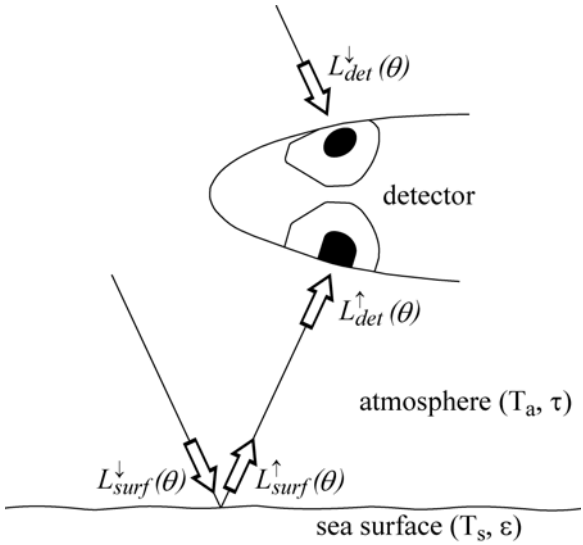

Figure 1. Schematic diagram of detector configuration for emissivity retrievals. Upwelling and downwelling radiances at view angle θ are combined to retrieve surface properties, after taking account of the atmospheric transmission. See text for details.

where $\rho(\mathbf{n}, \chi)$ is the reflectance dependent on the complex refractive index of water $\mathbf{n}$, meaning $n + ik$, and the angle of incidence χ of the light.

The emissivity for any realistic sea surface is more complicated due to the presence of waves, which introduce a degree of surface roughness. In this case the statistical distribution of slope angles of individual wave facets is required to calculate the overall emissivity at a given viewing angle (here and throughout the view angle is defined as the zenith angle from vertical). A well established sea surface emissivity model is that of Masuda *et al.* (1988) which incorporates the wind speed-dependent wave slope distribution derived by Cox and Munk (1954) from sun glitter observations. For view angles of less than 30°, however, there is no significant angular or wind speed dependence (except in very high wind speeds which lead to the generation of foam). Sufficiently high-resolution (1 cm^{-1} or better) radiometer measurements may be used to determine the emissivity of a water surface provided both the upwelling radiance and downwelling sky radiance are measured near-simultaneously. The discussion of the retrieval procedure that follows is similar to that formulated by Smith *et al.* (1996) and Fiedler and Bakan (1997).

Figure 1 shows a schematic view of the sensor configuration for an emissivity retrieval experiment conducted over ocean, with the radiometer viewing upwelling and downwelling radiances at the same small angle to the vertical. This is advantageous in that the cone of angles reflected by the rough sea into the radiometer field of view can be closely approximated by a single downwelling ray at the specular reflection angle. The radiance leaving the surface will comprise the thermal emission component plus the reflected incident radiation, i.e.

$$L^{\uparrow}_{\text{surf}}(\theta) = \varepsilon(\theta)B(T_s) + (1 - \varepsilon(\theta))L^{\downarrow}_{\text{surf}}(\theta), \tag{2}$$

where $\varepsilon(\theta)$ is the emissivity at zenith viewing angle θ, $B(T_s)$ is the Planck function at surface temperature T_s, $L^{\downarrow}_{\text{surf}}(\theta)$ is the downwelling radiance at the surface and all quantities in this and subsequent equations are spectrally dependent. The effect of the

intervening atmosphere between the radiometer and surface must be taken into account, since the atmospheric transmission properties will modulate the detected radiances. The upwelling radiance reaching the detector may therefore be expressed as:

$$\begin{aligned} L^{\uparrow}_{\mathrm{det}}(\theta) &= \tau(\theta) L^{\uparrow}_{\mathrm{surf}}(\theta) + E(\theta) \\ &= \tau(\theta) L^{\uparrow}_{\mathrm{surf}}(\theta) + (1 - \tau(\theta)) B(T_{\mathrm{a}}), \end{aligned} \tag{3}$$

where $E(\theta)$ is the atmospheric emission term, and $\tau(\theta)$ and T_{a} are the spectral transmittance and average atmospheric temperature between the instrument and water surface, respectively. Similarly the downward sky radiance at the surface may be rewritten as:

$$L^{\downarrow}_{\mathrm{surf}}(\theta) = \tau(\theta) L^{\downarrow}_{\mathrm{det}}(\theta) + (1 - \tau(\theta)) B(T_{\mathrm{a}}), \tag{4}$$

which is a second-order correction since only a small fraction of the sky radiance is reflected back to the detector.

Combining (2), (3) and (4) and solving for the emissivity leads to the relation:

$$\varepsilon = \frac{L^{\uparrow}_{\mathrm{det}} - \tau^2 L^{\downarrow}_{\mathrm{det}} - (1 - \tau^2) B(T_{\mathrm{a}})}{\tau \{ B(T_{\mathrm{s}}) - \tau L^{\downarrow}_{\mathrm{det}} - (1 - \tau) B(T_{\mathrm{a}}) \}}, \tag{5}$$

where the dependence on the view angle θ is implicit. Equation (5) is highly sensitive to the value of the radiometric skin temperature T_{s}, which must be determined to high accuracy. Smith *et al.* (1996) achieved this by inverting a version of (5) to solve for T_{s} at a wavelength where the non-black-body upwelling radiance was compensated by a relatively 'warm' sky radiance, so not needing a very accurate first estimate of ε.

We choose a slightly different route, by seeking to determine the surface temperature and emissivity simultaneously (Fiedler and Bakan 1997). It should be possible to find the fraction ρ such that:

$$L^{\uparrow}_{\mathrm{surf}} - \rho \cdot L^{\downarrow}_{\mathrm{surf}} = \varepsilon B(T_{\mathrm{s}}) \tag{6}$$

is a smooth function (i.e. contains no spectral structure from the sky radiance), where from (2) ρ is simply the reflectance of the surface, since the emissivity and Planck function both vary slowly with frequency. In practice ρ is determined over several wave number intervals, around 40 cm^{-1} wide, where the reflectance can be approximated as being constant. Making use of (3) and (4) to rewrite (6) as:

$$\frac{1}{\tau} \{ L^{\uparrow}_{\mathrm{det}} - (1 - \tau) B(T_{\mathrm{a}}) \} - \rho \cdot \{ \tau L^{\downarrow}_{\mathrm{det}} + (1 - \tau) B(T_{\mathrm{a}}) \} = \varepsilon B(T_{\mathrm{s}}), \tag{7}$$

ρ may be calculated from detected radiances, using a least-squares method to minimize the variance with respect to frequency of a quadratic fit to the left-hand side of (7) for each spectral interval. This requires that the ambient atmospheric temperature be known, for which the measured upwelling brightness temperature in an opaque region (such as the 15 μm CO_2 band) is accurate to within 0.2 K. (An error of 0.2 K in T_{a} results in an error of less than 0.0004 in retrieved emissivity.) An additional requirement is the atmospheric path transmittance τ, which is calculated using a line-by-line radiative transfer model. Dropsondes launched during flight provide us with information on the atmospheric state for the lowest part of the atmosphere for inclusion in the transmittance calculation. We estimate uncertainties in atmospheric path temperature and humidity of approximately 0.3 K and 5%, respectively, resulting in negligible emissivity errors due to the small transmittance correction (less than one part in 10^4). Having calculated ρ,

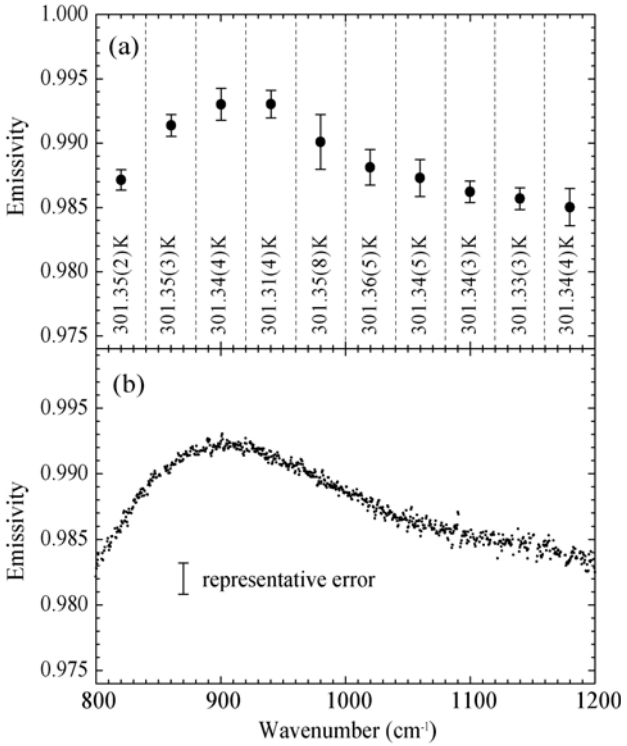

Figure 2. (a) Coarse-resolution retrieval from flight A670. The emissivity is determined over ten bands of width 40 cm^{-1}, with error bars showing the standard deviation among 45 separate nadir spectra recorded during the aircraft run. The skin temperature is retrieved simultaneously, with values given for each band (the standard deviation of the last digit is included in parentheses). (b) A best estimate of the skin temperature, in this case 301.34 K, is used to infer the emissivity at full ARIES resolution, shown as a scatter plot of individual spectral data points. The error bar shows the reproducibility of the retrieval, approximately ±0.001.

and thereby ε, the surface temperature T_s is found by inverting the Planck function inferred from (5). This method will generate a coarse-resolution set of emissivity values as a function of wave number, each with a separate estimate of T_s (see Fig. 2). The mean value of T_s may then be included directly in (5) to calculate the emissivity at full spectral resolution.

The theory presented above allows us to use field measurements of upwelling and downwelling infrared radiances to retrieve directly the emissivity of a water surface. In this work we present interferometer emissivity retrievals from two sources. In section 3 we describe measurements conducted over the real ocean from two aircraft campaigns, while in section 4 ground-based measurements using an artificial sea surface are detailed.

3. Aircraft measurements

The aircraft data presented here were collected during two Measurement Of Tropospheric Humidity (MOTH) campaigns, the first located in the tropical South Atlantic during April–May 1999 and the second over the Baltic Sea in December 1999. Infrared radiances were recorded using the Airborne Research Interferometer Evaluation System (ARIES, see Wilson *et al.* 1999) which was mounted in an under-wing pod on the Met

Office Hercules C-130 aircraft. Observations were conducted at an altitude of approximately 35 m above the ocean. ARIES was directed to view nadir (upwelling) and zenith (downwelling) radiances, i.e. at 0° and 180° to the surface, using the full optical path difference of the interferometer (0.482 cm^{-1} sample spacing).

We need to correct the measured radiances for the influence of the low-flying aircraft. ARIES views a small area of the ocean surface, but because the surface is roughened by wind the reflected downwelling radiation originates from a spread of angles. A proportion of the reflected rays reaching ARIES may emanate from the overflying aircraft rather than from the sky; in this case the measured downwelling radiance will not be representative of the actual reflected radiance. Our correction scheme includes a Monte Carlo simulation of sea surface facets following the methodology of Watts *et al.* (1996). Each facet in the ensemble is generated according to the probability distribution of Cox and Munk (1954), accounting for the projected area displayed by the facet to the direction of view. The resulting set of angles is weighted by the Fresnel reflectance of each facet to give the distribution of rays, which are then mapped onto the horizontal plane containing the aircraft to calculate the fraction of rays emanating from it. The simulation takes as input the masthead (12.5 m) wind speed that determines the distribution of wave slope angles in the Cox and Munk model, as well as the aircraft height above the surface and the aircraft pitch angle. (The nose of the C-130 is invariably 'pitched up' during level flight, which means ARIES views an area on the sea surface slightly forward of the interferometer.) Figure 3 shows an example of such a calculation for flight A670; it is apparent that part of the reflected radiation does indeed originate from the underside of the aircraft, typically between 10% and 14% in our simulations (depending mainly on wind speed). This fraction of the measured downwelling radiance is replaced by black-body thermal emission at the ambient atmospheric temperature to represent the aircraft skin.

The emissivity retrieval proceeds as described in section 2. Figure 2(a) shows data from a straight and level run over the South Atlantic. There is great consistency among the ten estimates of the skin temperature, with a spread of only 0.05 K. The best (average) estimate of the surface temperature is then used to derive the emissivity at full spectral resolution, shown in Fig. 2(b). The scatter results from instrument noise and inaccuracies in the retrieval method, e.g. uncertainties in the atmospheric transmission due to water vapour below the aircraft. A small number of data points, those falling below a transmission threshold of $\tau = 0.95$, are omitted as the retrievals here are subject to significant errors. There is a trade-off in thermal emission between the surface temperature (through the Planck function) and the emissivity, and as Fig. 2 shows a small spread in SST is associated with a larger range of emissivity values in percentage terms.

Emissivity spectra retrieved from two clear-sky flights, A670 and A676, have been combined to derive a best (average) emissivity for the South Atlantic, shown in Fig. 4. The figure compares measurements with model calculations, applying the formulae of Masuda *et al.* (1988), using refractive index data taken from the literature. A calculation with a complex refractive index due to Hale and Querry (1973) (adjusted for the salt correction of Friedman 1969) is shown in the top panel in Fig. 4(a), in good agreement with the observed data. The middle panel shows the difference between measured and modelled spectral emissivities, which in this case is generally less than the estimated measurement uncertainty of $\pm$ 0.001. With reference to (5), the choice of model emissivity directly affects the surface temperature derived by inverting the Planck function $B(T_s)$. In the lower panel in Fig. 4(a) T_s has been determined spectrally from (5) by combining detected radiances and atmospheric emission terms for flight A670.

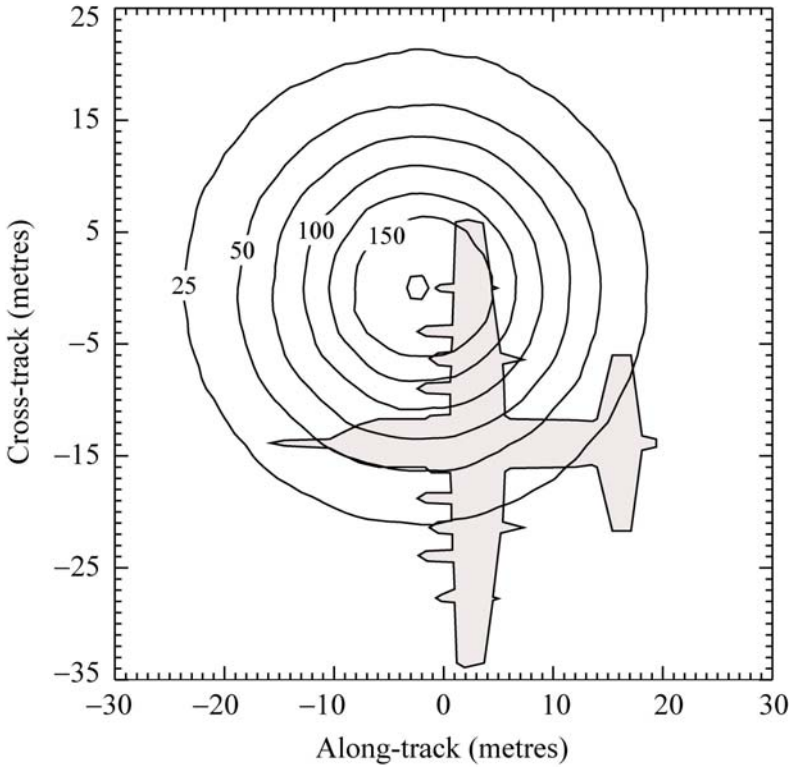

Figure 3. Contours showing the distribution of rays reflected from a rough ocean into the ARIES field of view at an aircraft altitude of 35 m. A total of 5×10^6 wave facets have been included in the Monte Carlo simulation with a 12.5 m wind speed of 7.7 ms^{-1}. The contour scale is reflectance per square metre, multiplied by 5×10^6.

While the retrieval itself produces a surface skin temperature of 301.34 K, assuming the model emissivity results in a slightly lower temperature of 301.32 K, due to it being slightly higher than the measured emissivity. The spectral dependence of the derived skin temperature is insignificant. Figures 4(b) and (c) repeat these results but with model emissivities calculated using the salinity-corrected refractive indices of Downing and Williams (1975) and Bertie and Lan (1996), respectively. The data of Bertie and Lan produce the greatest discrepancy between measurement and theory, with the resultant SST now dependent on wave number.

We present in Fig. 5 data recorded over the Baltic Sea, repeating the analysis for three sets of published refractive indices. Due to freshwater inflows, the salinity of the Baltic Sea is relatively low; in the region of the aircraft campaign we expect a surface salinity 25% of that of the open ocean (Samuelsson 1996). Therefore we adjust the pure-water refractive indices by a fraction 0.25 of that suggested by Friedman (1969). Comparing Figs. 4 and 5 it is clear that the retrieved emissivity over the Baltic Sea is significantly different from that measured over the South Atlantic. The calculated emissivity is significantly higher than that measured, particularly from 760–900 cm^{-1} in Figs. 5(a) and (b). This results in an inferred SST as much as 0.3 K below that retrieved, if the calculated emissivities are assumed. The complex refractive index of Bertie and Lan (1996) fares better at reproducing at least the spectral shape of the measured emissivity, as shown in Fig. 5(c); there is, however, still a bias in emissivity of around 0.0025 across the atmospheric window, which gives an inferred SST at least 0.1 K lower

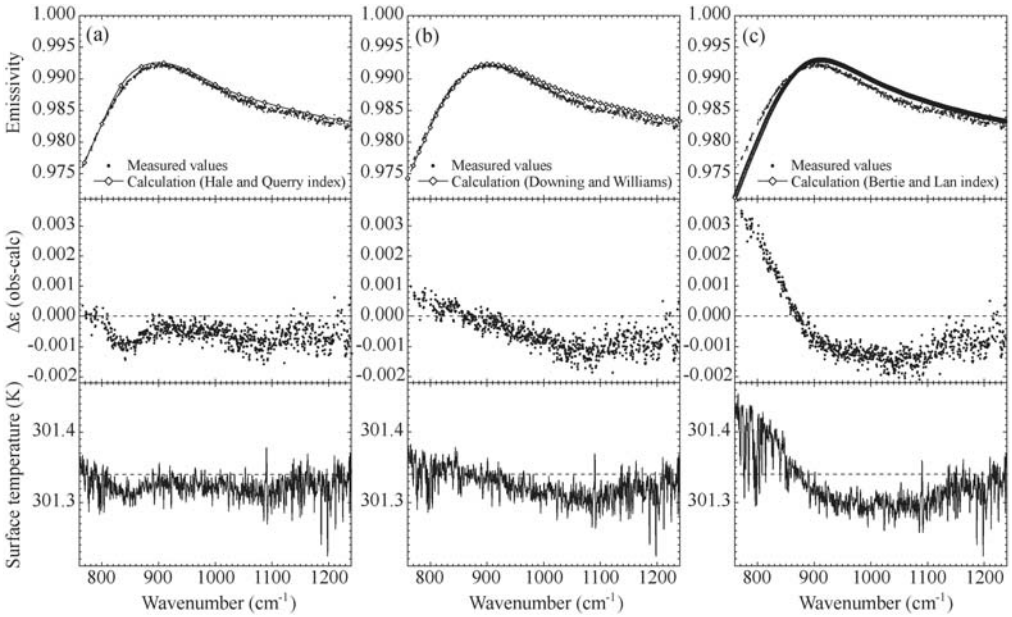

Figure 4. Emissivity retrieval for the South Atlantic compared with model calculations using refractive indices from: (a) Hale and Querry (1973), (b) Downing and Williams (1975) and (c) Bertie and Lan (1996). In each case the top panel shows the retrieved and model emissivity, the middle panel shows the observed minus calculated residual, and the lower panel shows the inferred spectral surface skin temperature derived assuming the model emissivity (retrieval skin temperature shown as the dotted line).

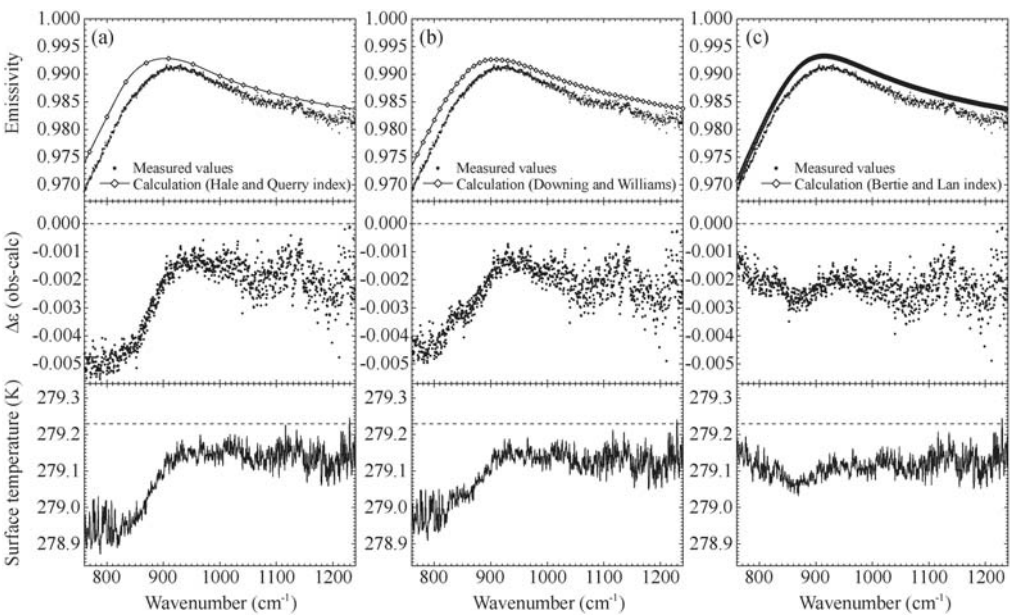

Figure 5. As Fig. 4, but for retrieved emissivity from flights over the Baltic Sea.

than that retrieved with the ARIES measurements. Note that the salinity correction to the refractive indices results mainly in a small frequency shift rather than a vertical scaling of the emissivity, and on its own cannot explain the difference between Figs. 4 and 5. It is not possible from these results alone to determine which of the literature refractive indices is best able to represent the emission properties of the global ocean, or whether differences in temperature or salinity (or both) are important determinants of the emissivity.

4. Ground-based measurements

To supplement the aircraft measurements outlined in the previous section, and assess the impact of temperature and salinity changes, further measurements were undertaken on the ground using ARIES to view a calm water reservoir with varying characteristics. Whereas Cox and Munk (1954) predict the presence of ocean wave slopes even at zero wind speed, the flat water surface in our experiments may be described simply by Fresnel's relations for emissivity. The measurements are therefore a test of refractive index rather than emissivity model.

A digital photograph and scale diagram of the apparatus is displayed in Fig. 6. ARIES was supported in a cradle mounted on an aircraft nose cone, which allowed views of the water surface at an angle of 50° to the vertical. An ultrasound bath contained the water sample, which was heated or cooled to stable temperatures of approximately 0, 10, 20 and 30 °C. ARIES was directed to view the water surface at each temperature for approximately five minutes, followed by an associated measurement of the sky radiance at the reflection angle of 50°. A series of measurements over four temperatures was performed, initially with the bath containing pure deionized water, followed by additions of salt (Sigma–Aldrich product S9883) dissolved to simulate seawater with half (17.5 g l^{-1}) and full (35 g l^{-1}) standard ocean salinity. A number of platinum resistance thermometers (PRTs) were used to monitor the water bath temperature with depth. The ultrasound bath could be operated to agitate the water and so circumvent the skin effect, whereby a temperature gradient is established in the uppermost surface layer due to differential heating or cooling. It was found that the agitation produced surface ripples, but these appeared not to affect retrieved emissivity values which were indistinguishable from those recorded with the ultrasound not operating. Since the radiometric surface temperature inferred from ARIES is in any case more accurate than using the PRTs, the surface cooling is unimportant so long as the emissivity and temperature are determined simultaneously.

Figure 7(a) presents emissivity spectra retrieved for pure water over four temperatures between 273.7–300.5 K (0.5 and 27.4 °C). We choose to compare our retrievals against Fresnel calculations using the complex refractive index of Downing and Williams (1975), since this was measured at 300 K and gives the best agreement with our data at this temperature. It is immediately clear that the emissivity is indeed dependent on temperature, most markedly around 760–830 cm^{-1} where there is a spread of 0.008 (or 0.8%) in retrieved values over a temperature range of 27 K. Whereas the agreement with model calculations is very good for pure water at 300 K, residual errors become progressively larger as the temperature decreases. The combination of several small sources of error (uncertainty in view angle (±0.5°), reproducibility errors resulting from instrument noise and/or a variable sky radiance, uncertainties in atmospheric emission and in the polarization sensitivity of ARIES) results in an overall propagated uncertainty in emissivity retrievals, varying with frequency, of between 0.0009 (at 920 cm^{-1}) and 0.0016 (at 760 cm^{-1}). Since the estimated measurement error

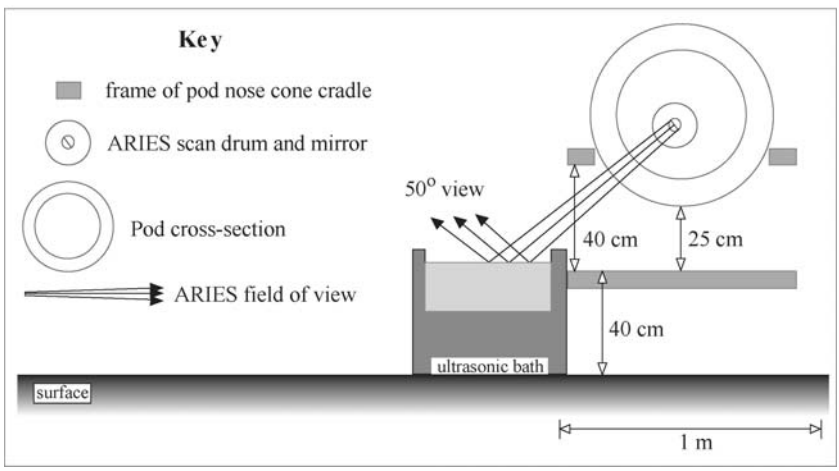

Figure 6. Digital photograph and scale diagram of the experimental set-up for the ground-based emissivity experiments.

is far exceeded by the range of emissivity in Fig. 7(a), we conclude that the temperature dependence is a real effect and not an artefact of our retrieval procedure.

Figure 7(b) estimates the impact on a notional retrieved SST of assuming a temperature-independent emissivity for pure-water data at 300.5 and 273.7 K. At 300.5 K the surface temperature derived assuming the Fresnel (Downing and Williams 1975) emissivity is insensitive to channel wave number, and is within hundredths of a degree of the retrieved value. By contrast, at 273.7 K adopting the model emissivity leads to deviations in SST of up to 0.5 K, with the most significant discrepancies found in the 760–840 cm^{-1} region. Note that relatively strong water vapour lines around 800 cm^{-1} serve to decrease the impact of a variable emissivity, since at these frequencies

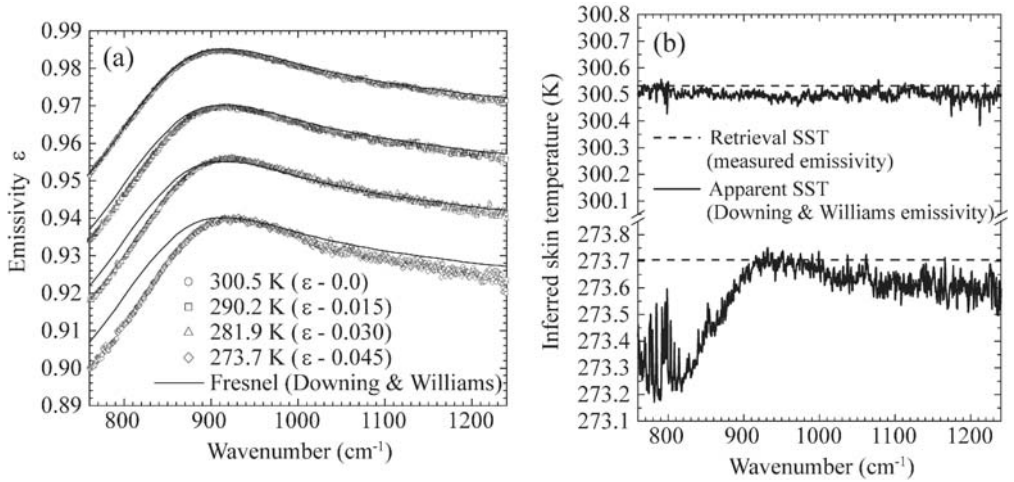

Figure 7. (a) ARIES retrievals viewing a pure, de-ionized water surface at four temperatures (symbols, see legend) compared with Fresnel calculations using the complex refractive index of Downing and Williams (1975); the curves have been offset vertically by shown increments, ε, for clarity. (b) Inferred sea surface skin temperatures (SSTs) assuming calculated Fresnel emissivity (dashed lines show retrieval temperatures) for the hottest and coldest water samples at 300.5 K and 273.7 K.

the downwelling radiance originates from lower, warmer regions of the atmosphere so partially compensating for the non-unity emissivity of the water surface. The choice of refractive index makes some difference to estimates of the SST bias; for instance, using the data of Bertie and Lan (1996) results in smaller biases at the coldest temperatures but introduces larger biases at 300.5 K.

In order to isolate the effect of salinity on emissivity, differences in temperature between comparable measurements (due to the difficulty in achieving a precise target bath temperature) should be eliminated. It appears from Fig. 7 that the variation in emissivity is a smooth function of temperature, and therefore we interpolate between measurements at adjacent temperatures to obtain normalized emissivity spectra at the desired temperature. The effective temperatures for salinity comparisons were chosen to be 275, 283, 291 and 300 K. Emissivity corrections due to temperature normalization were in all cases small.

Figure 8 shows retrieved emissivity spectra with salinities of 0, 17.5 and 35 g l^{-1} for water skin temperatures of (a) 300 and (b) 275 K, compared with reference Fresnel calculations using the refractive index of Downing and Williams (1975; valid for zero salinity and a temperature of 300 K). The trend of emissivity with salinity appears to be consistent with that described by Friedman (1969) who observed a shift in transmittance of approximately -4 cm^{-1} for standard ocean salinity relative to pure water. The effect of salinity is, therefore, to increase the emissivity over pure-water values below 900 cm^{-1} and decrease it above 900 cm^{-1}. It should be noted that the uncertainties, represented as error bars in Fig. 8 at four frequencies, are comparable in size to the change in emissivity that results from salinity variation. Bearing in mind that the range of surface open ocean salinity rarely exceeds 33–37 g l^{-1}, the variability of emissivity due to salinity can be considered negligible once corrections to pure-water values have been made.

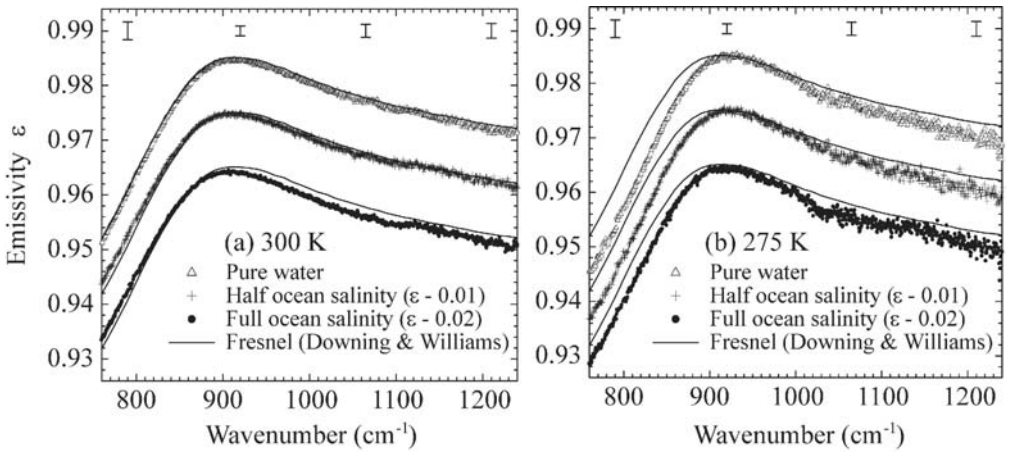

Figure 8. Salinity dependence of emissivity at (a) 300 K and (b) 275 K, for pure water and half and full salinity solutions versus a standard pure-water calculation (Downing and Williams 1975). Error bars are representative of the uncertainty at four points across the atmospheric window. The curves have been offset by shown increments, ε, for clarity.

The most widely adopted salinity correction applied to pure-water refractive indices is that due to Friedman (1969). A subsequent study by Pinkley and Williams (1976) found general agreement with Friedman's values but did not tabulate their results. In order to examine the work of Pinkley and Williams, refractive index corrections have been transcribed from figures contained in their paper. In Fig. 9 we compare the emissivity *difference* (measured saline minus pure-water emissivity) over four temperatures against the difference that results from using the correction schemes of Friedman (1969) and Pinkley and Williams (1976). Fresnel calculations have been performed for a 50° view angle using the refractive index of Downing and Williams (1975) to derive the model difference, though the choice of index does not significantly affect the results. The data for the four temperatures show a consistent trend with wave number, though there is considerable scatter; since this is a difference plot the uncertainties are up to twice those shown in Fig. 8. There appears to be no particular trend of salinity correction with temperature. Comparing the correction scheme due to Friedman with that of Pinkley and Williams the two are similar in their effect, though the latter has more spectral variation. In particular the data of Pinkley and Williams include the localized effects of an absorption peak due to sulphate ions around 1100 cm^{-1}, which causes a change in shape of the spectral emissivity. Given the experimental uncertainties it is not possible to assess definitively the respective accuracies of the two refractive index salinity corrections. In the remainder of this paper we adopt the scheme due to Friedman (1969), since this is most widely used and is generally in good agreement with our data.

We have analysed the dependence of emissivity on salinity and temperature in the 8–13 μm window region. In the ARIES spectral range the regions around 2000–2200 cm^{-1} and 2500–3000 cm^{-1} are sufficiently transparent to be useful for surface remote sensing. Unfortunately, due to the decline in magnitude of the thermal emission signal at higher frequencies, emissivity retrievals in these regions are subject to much higher errors than at 8–13 μm. Although retrievals of emissivity in the 2050–2150 cm^{-1} range, giving values between 0.963 and 0.970, are broadly in line with model values, no meaningful data on temperature or salinity dependency could be obtained.

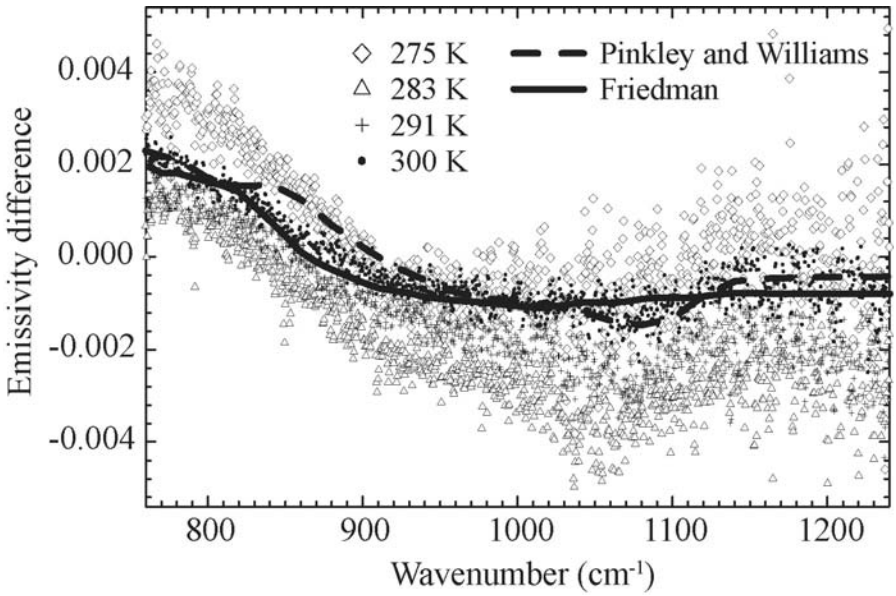

Figure 9. Measured difference in emissivity (standard ocean salinity minus pure-water cases) for the four temperatures measured, symbols as shown in the legend. Also shown are model differences using the salinity correction schemes of Friedman (1969, solid line) and Pinkley and Williams (1976, dashed line).

5. Derivation of complex refractive indices

It is not possible to infer the refractive index of water, $n + ik$, from measurements of emissivity (or reflectance) at one angle, since both the real and imaginary components are unknown variables that determine the result. However, with measurements at two or more angles a solution may be found, and we may use our measurements of emissivity at angles of 0° (from the aircraft) and 50° (on the ground) to determine n and k for sea water. Since the Fresnel equations are valid for a flat water surface, and the aircraft measurements were performed over a wind-ruffled sea surface, account should be taken of the effect of surface roughness. In fact at near-nadir viewing angles the presence of waves affects the emissivity very little (Masuda *et al.* 1988). Nevertheless these corrections have been applied to our aircraft measurements for consistency in order to derive flat-surface values.

The emissivity results we use are normalized to standard conditions of salinity and temperature. For salinity we have measurements for sea water (35 g l^{-1} dissolved salts) for all cases except flights over the Baltic Sea. A partial correction following Friedman (1969) has been applied to these data. We choose the temperatures of the aircraft measurements as our standard conditions, namely 301.2 K (28.1 °C) for data collected over the South Atlantic and 279.0 K (5.9 °C) over the Baltic Sea. Ground-based measurements of artificial sea water were interpolated to these temperatures in a similar manner to that outlined before. We assume there are no environmental factors such as the presence of foam or other impurities that might affect the measured emissivity from the aircraft in a way that is absent from the ground-based measurements. Watts *et al.* (1996), drawing on reflectance measurements by Salisbury *et al.* (1993), estimated that only for wind speeds >15 m s^{-1} would current model schemes be invalidated by the presence of foam.

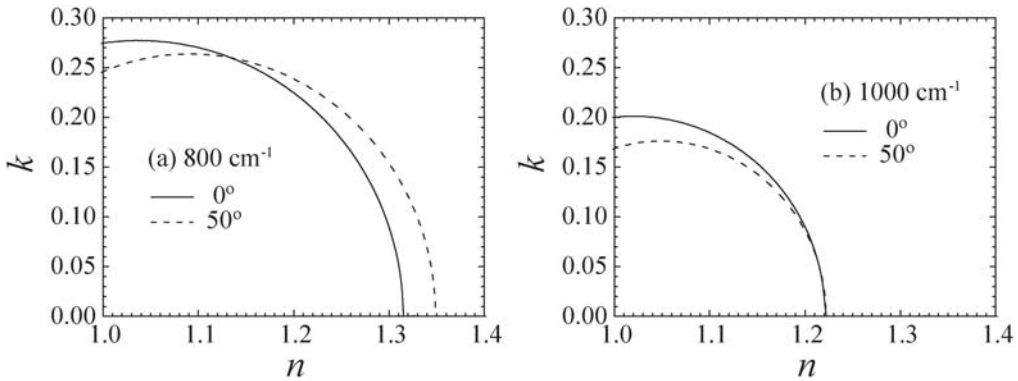

Figure 10. Possible solutions for real (n) and complex (k) parts of the refractive index given the Fresnel emissivity at angles of 0° and 50° (solid and dashed lines, respectively). The intersection of the curves gives the solution for n and k: (a) at 800 cm^{-1} values of $n = 1.134$, $k = 0.26$ were used to calculate the emissivity values; (b) at 1000 cm^{-1}, $n = 1.214$, $k = 0.0534$ (taken from Downing and Williams (1975)).

For the purposes of this paper we use the equations given in Sidran (1981) that relate the polarized components of emissivity to the real and imaginary parts of the refractive index. The total measured emissivity is simply the average of the two components for an unbiased radiometer. Put simply, there is a range of possible n and k that can reproduce measured emissivities at the two angles, 0° and 50°. In (n, k) space the possible values are curves that intersect at the solution, as shown in Fig. 10. The figure illustrates the point that solutions are more easily arrived at when the imaginary part k is significantly above zero. This is true around 800 cm^{-1} where the intersection of the curves is straightforwardly identified. Beyond 1000 cm^{-1}, however, k becomes very small, and the curves have a grazing intersection that is very sensitive to the input emissivity values. Indeed, if measurement errors are taken into account the curves may not intersect at all. We constrain k to zero in these circumstances.

With emissivity spectra at two view angles and two temperatures the above approach was used to calculate effective n and k, shown in Fig. 11. To reduce the effects of noise in the retrievals the emissivities were smoothed and re-gridded to a resolution of 10 cm^{-1}. The error bounds shown in Fig. 11 represent the inclusion of estimated errors in emissivity, with uncertainties of around 1% in emissivity translating into a significant range of n, k values. While n is derived with greater precision as wave number increases across the window, values of k become almost meaningless above 900 cm^{-1} as the imaginary part becomes small. Importantly, however, k is calculated to seemingly high precision in the region 770–840 cm^{-1} where values are highest. There appears to be a trend of increasing refractive index (for both components n and k) as the temperature falls from 301 to 279 K. At 279 K the peak of real index n at 860 cm^{-1} is a spurious feature caused by a missed intersection (refer to Fig. 10): k is set to zero, below its true value, and n is forced to be too high in compensation.

Published values of the complex refractive index show a consistent trend, namely a minimum in the real refractive index around 830 cm^{-1} and a steady decline in the imaginary part from 700 to 1240 cm^{-1}. It is reasonable, therefore, to use these established characteristics as physical constraints on our derived indices. We also note that above 1000 cm^{-1} the imaginary part of the refractive index is so small as to have little impact on the overall computed emissivity, with the real part dominating the calculation. With these justifications in mind we adapt published imaginary indices

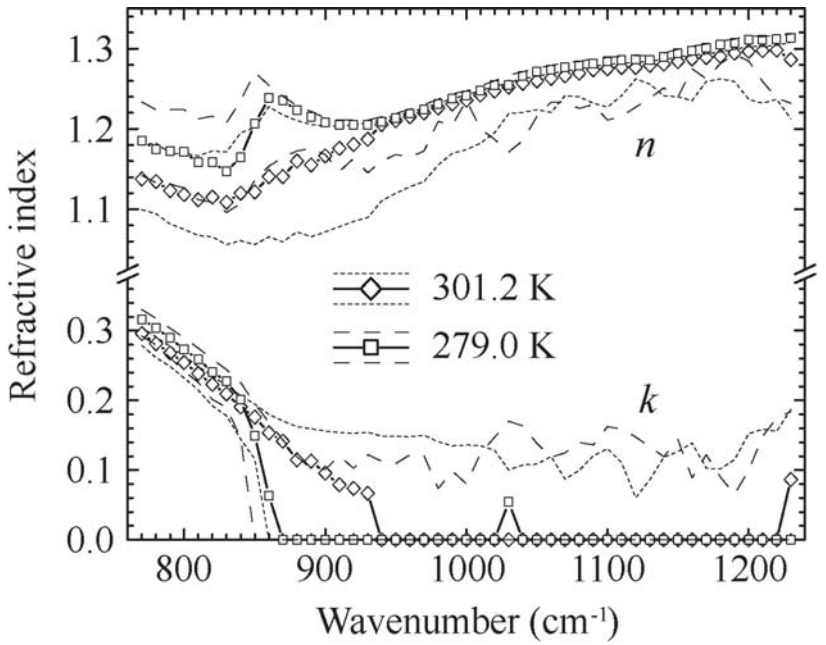

Figure 11. Values of real (n) and complex (k) parts of the refractive index derived from measured emissivity data at reference temperatures of 301.2 K and 279.0 K with associated error bounds (see legend). Where the data give no solution (no intersection of the curves as shown in Fig. 10) k has been set to zero.

to correct our derived values within the uncertainty shown in Fig. 11. Published values of k show a great degree of consistency, with the exception of the work of Bertie and Lan (1996). We choose as a reference the compilation of Hale and Querry (1973). This imaginary index agrees with our derived values below 940 cm^{-1} for the 301 K case, and we extend our values of k above 940 cm^{-1} by replicating the values of Hale and Querry. For the 279 K case our derived k at low wave numbers agrees with published values of Hale and Querry if the latter are multiplied by a constant factor 1.09. These adjusted indices are substituted for those measured above 850 cm^{-1} and n recomputed from measured emissivity spectra. Final values for n and k at the two temperatures are presented in Table 1.

We seek to generalize these results to obtain a refractive index that is applicable at any chosen temperature. If n and k vary linearly with temperature T (as the evidence from experiments suggests, see Fig. 7) then we have the relationships:

$$n = n_0 + c_n(T - 273.15\ \mathrm{K}) \tag{8a}$$

and

$$k = k_0 + c_k(T - 273.15\ \mathrm{K}), \tag{8b}$$

where n_0 and k_0 are the real and imaginary indices at 273.15 K, and c_n and c_k are to be determined empirically. In general these four variables will be functions of frequency. It is straightforward to fit our values of n and k at 279.0 K and 301.2 K to obtain these parameters, which are detailed in Table 1.

Figure 12 compares the derived complex indices with values from the literature. These pure-water laboratory data were nearly all obtained at room temperature, and a salt correction has been applied following Friedman (1969). Exceptionally, the data of Pinkley *et al.* (1977) are temperature-dependent values measured at 1, 16 and 39 °C.

TABLE 1. DERIVED COMPLEX REFRACTIVE INDICES[1] AT 301.2 AND 279.0 K, AND COEFFICIENTS FOR EQS. (8a,b)

Wave number (cm^{-1})	n (at 301.2 K)	k (at 301.2 K)	n (at 279.0 K)	k (at 279.0 K)	n_0	k_0	c_n	c_k
770	1.1375	0.2959	1.1860	0.3162	1.1988	0.3216	−0.0021861	−0.0009139
780	1.1350	0.2816	1.1748	0.3044	1.1852	0.3104	−0.0017897	−0.0010253
790	1.1231	0.2682	1.1723	0.2892	1.1853	0.2948	−0.0022182	−0.0009457
800	1.1189	0.2543	1.1710	0.2735	1.1847	0.2786	−0.0023449	−0.0008654
810	1.1124	0.2388	1.1587	0.2589	1.1709	0.2642	−0.0020828	−0.0009049
820	1.1156	0.2230	1.1583	0.2409	1.1695	0.2456	−0.0019205	−0.0008071
830	1.1087	0.2091	1.1474	0.2271	1.1576	0.2319	−0.0017444	−0.0008102
840	1.1204	0.1905	1.1646	0.2012	1.1763	0.2040	−0.0019929	−0.0004817
850	1.1215	0.1763	1.1726	0.1791	1.1860	0.1798	−0.0023028	−0.0001245
860	1.1410	0.1535	1.1684	0.1639	1.1757	0.1666	−0.0012373	−0.0004662
870	1.1408	0.1415	1.1665	0.1493	1.1733	0.1513	−0.0011579	−0.0003507
880	1.1600	0.1146	1.1650	0.1356	1.1663	0.1411	−0.0002259	−0.0009457
890	1.1552	0.1128	1.1673	0.1226	1.1705	0.1251	−0.0005459	−0.0004387
900	1.1665	0.0956	1.1677	0.1113	1.1680	0.1154	−0.0000525	−0.0007070
910	1.1762	0.0790	1.1717	0.1013	1.1705	0.1072	0.0002023	−0.0010059
920	1.1809	0.0737	1.1780	0.0919	1.1772	0.0967	0.0001313	−0.0008194
930	1.1871	0.0665	1.1828	0.0839	1.1816	0.0885	0.0001956	−0.0007845
940	1.1901	0.0709	1.1907	0.0773	1.1909	0.0790	−0.0000313	−0.0002875
950	1.1978	0.0654	1.1979	0.0713	1.1979	0.0729	−0.0000045	−0.0002652
960	1.2036	0.0606	1.2061	0.0661	1.2067	0.0675	−0.0001104	−0.0002458
970	1.2110	0.0566	1.2131	0.0617	1.2137	0.0631	−0.0000973	−0.0002297
980	1.2180	0.0534	1.2216	0.0582	1.2225	0.0595	−0.0001621	−0.0002165
990	1.2243	0.0513	1.2294	0.0559	1.2308	0.0571	−0.0002309	−0.0002080
1000	1.2294	0.0498	1.2333	0.0543	1.2343	0.0555	−0.0001743	−0.0002019
1010	1.2352	0.0482	1.2408	0.0526	1.2422	0.0537	−0.0002493	−0.0001956
1020	1.2412	0.0470	1.2475	0.0512	1.2491	0.0523	−0.0002813	−0.0001903
1030	1.2457	0.0457	1.2554	0.0498	1.2579	0.0509	−0.0004351	−0.0001854
1040	1.2512	0.0446	1.2597	0.0486	1.2619	0.0497	−0.0003829	−0.0001807
1050	1.2551	0.0436	1.2649	0.0475	1.2675	0.0485	−0.0004440	−0.0001766
1060	1.2584	0.0426	1.2681	0.0465	1.2706	0.0475	−0.0004375	−0.0001728
1070	1.2614	0.0418	1.2718	0.0456	1.2746	0.0465	−0.0004699	−0.0001694
1080	1.2653	0.0410	1.2744	0.0447	1.2767	0.0457	−0.0004077	−0.0001663
1090	1.2693	0.0403	1.2767	0.0439	1.2786	0.0449	−0.0003341	−0.0001633
1100	1.2708	0.0396	1.2791	0.0432	1.2813	0.0441	−0.0003718	−0.0001605
1110	1.2727	0.0390	1.2803	0.0425	1.2823	0.0434	−0.0003433	−0.0001580
1120	1.2726	0.0384	1.2814	0.0418	1.2837	0.0427	−0.0003945	−0.0001556
1130	1.2752	0.0378	1.2818	0.0412	1.2835	0.0421	−0.0002957	−0.0001534
1140	1.2770	0.0373	1.2853	0.0407	1.2875	0.0416	−0.0003766	−0.0001513
1150	1.2801	0.0368	1.2899	0.0401	1.2925	0.0410	−0.0004425	−0.0001492
1160	1.2833	0.0363	1.2939	0.0396	1.2967	0.0405	−0.0004747	−0.0001473
1170	1.2852	0.0359	1.2972	0.0391	1.3003	0.0400	−0.0005377	−0.0001455
1180	1.2880	0.0355	1.3006	0.0387	1.3039	0.0395	−0.0005668	−0.0001439
1190	1.2912	0.0351	1.3037	0.0383	1.3070	0.0391	−0.0005633	−0.0001424
1200	1.2935	0.0348	1.3074	0.0379	1.3110	0.0387	−0.0006237	−0.0001409
1210	1.2942	0.0344	1.3077	0.0375	1.3112	0.0383	−0.0006046	−0.0001395
1220	1.2951	0.0341	1.3082	0.0372	1.3117	0.0380	−0.0005934	−0.0001382
1230	1.2995	0.0338	1.3099	0.0368	1.3127	0.0376	−0.0004683	−0.0001370

[1]The refractive index of water is given by $n + ik$, and n_0 and k_0 are the real and imaginary indices at 273.15 K.

As such, these indices offer important corroboration of our results, showing a similar (and smooth) trend of increasing n, k with decreasing temperature.

The key requirement for our derived complex refractive index is to reproduce experimental emissivities within the measurement uncertainty, which is the case for the South Atlantic, Baltic Sea and ground-based results presented here. As an additional check on the validity of a linear scaling between temperatures, another set of measurements conducted south-west of Wales was considered (flight A711 on 13 September 1999) with a moderate ocean temperature of 288.6 K (15.5 °C). Figure 13 shows an emissivity

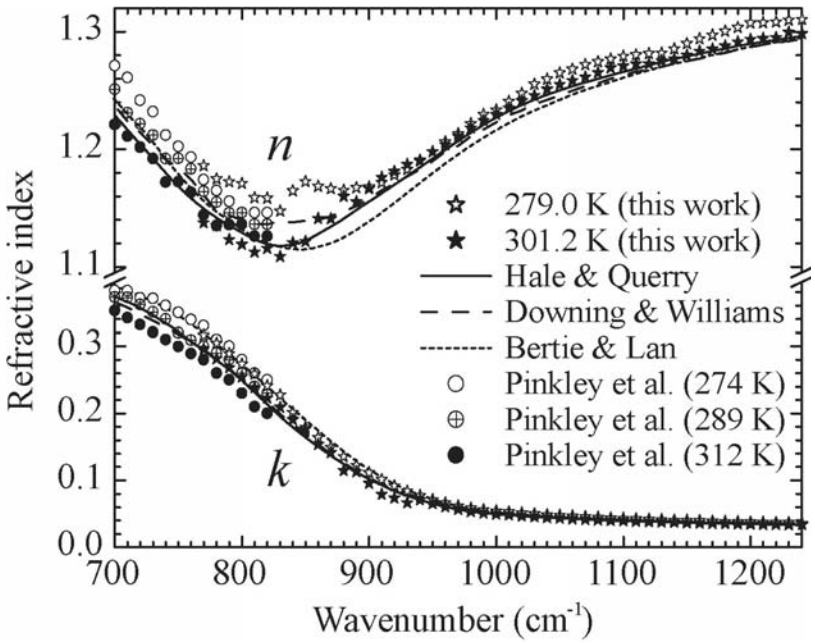

Figure 12. Derived values of real (n) and complex (k) parts of the refractive index from this work compared with salinity-corrected values from Hale and Querry (1973), Downing and Williams (1975), Bertie and Lan (1996) and Pinkley *et al.* (1977).

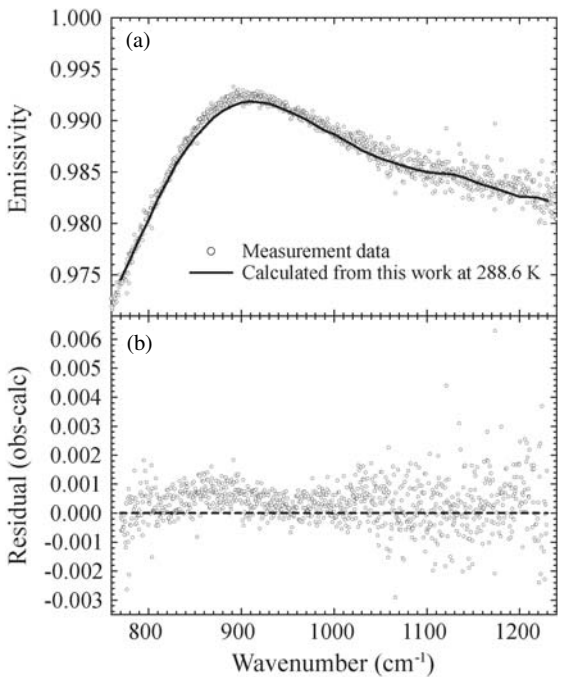

Figure 13. (a) Retrieved emissivity for flight A711 (see legend) together with a calculation using the refractive index given in Table 1, and (b) residual differences between observed and calculated values.

retrieval from this flight together with a calculation using (8a) and (8b). The agreement is close, and is further evidence of a smooth and gradual trend of sea water optical properties with temperature.

6. Impact on satellite SST retrievals

It is pertinent to assess the possible impact of our emissivity results on SST retrievals from satellite instruments. Simulated radiances have been calculated using the GENLN2 line-by-line radiative transfer code (Edwards 1992) for a number of atmospheric profiles. A range of surface emissivity values has also been explored, calculated from the formulae of Masuda *et al.* (1988) at zero wind speed for inclusion in the code. We consider the transparent window regions where we have temperature-dependent emissivity data, i.e. 770–1230 cm^{-1} (using (8a) and (8b) from this work) and 2650–3000 cm^{-1} (Pinkley *et al.* (1977), interpolating between temperatures as necessary). Emissivity values were generated at angles of 0° and 55° to represent nadir and slanted satellite viewing geometries. Although in principle surface roughness will strongly perturb the emissivity at 55°, compensating errors tend to make zero wind speed a reasonable approximation (Watts *et al.* 1996).

Four test cases were considered: a standard tropical profile (Anderson *et al.* 1986) with a SST of 300 K; a midlatitude summer profile, SST = 287 K; a midlatitude winter profile, SST = 274 K; and a subarctic* winter profile, SST = 274 K. The last two cases were included to investigate the effect of different water vapour column amounts for the coldest surface temperatures. Highly resolved line-by-line output was degraded to the spectral resolution of ARIES (approximately 1 cm^{-1}). Calculated upwelling and downwelling radiances, incorporating a temperature-dependent emissivity, have been combined to retrieve apparent SSTs. This is done via inversion of (2) assuming the tabulated emissivity of Masuda *et al.* (1988) as a standard temperature-independent formulation. Figure 14 shows results for both view angles, with the SST bias calculated as the inferred SST minus the true model SST. The bias is generally negative, as the emissivity is assumed to be too high in all cases except that at 300 K.

As expected, errors in SST are highest for the coldest skin temperatures (274 K) and in spectral regions where the emissivity shows greatest temperature dependence (below 900 cm^{-1}). Importantly, the SST bias is significantly greater at 55° than at 0°, by a factor of about 1.5, which implies it is especially important to specify the emissivity accurately at large viewing angles for high-resolution sounding. It appears that surface temperature is the overriding factor in determining the SST bias, as the midlatitude winter and subarctic winter profiles (both with surfaces of 274 K) show very similar results. In between spectral lines the SST bias reaches a maximum of −0.37 K at 0° and −0.58 K at 55°, both for subarctic cases. In the short-wave region above 2700 cm^{-1}, assuming the results of Pinkley *et al.* (1977) are valid the temperature dependency is much less significant, with biases not exceeding −0.1 K. Future work will focus on whether it is possible to separate any bias in satellite SST fields due to emissivity from other possible biases such as water vapour transmittance errors and the presence of clouds and dust, particularly in relation to AIRS and IASI. Additionally there is evidence that using a temperature-dependent emissivity may eliminate some of the global bias, approximately 0.2 K, that currently exists between two- and three-channel SSTs retrieved from the Along Track Scanning Radiometer (ATSR, Merchant 2005).

* Regions outside of but closely bordering the arctic circle and exhibiting cold, dry atmospheric characteristics. Profiles are defined precisely by Anderson *et al.* (1986).

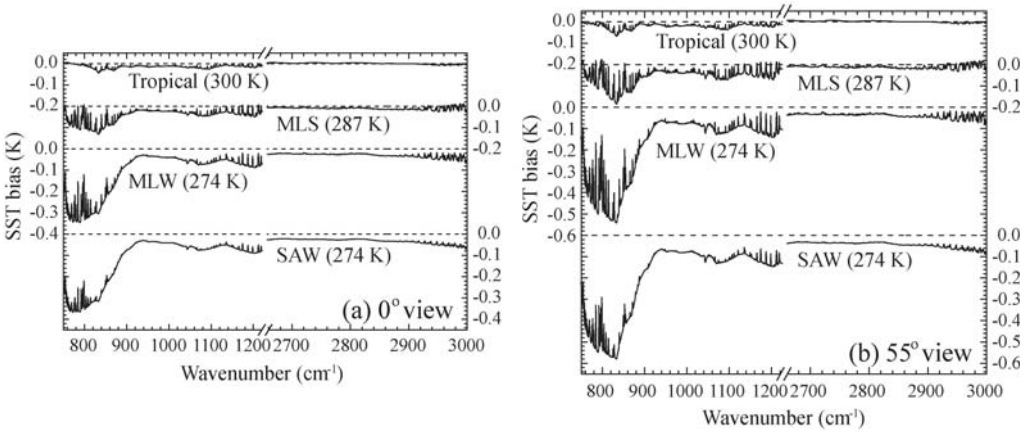

Figure 14. Calculations of the spectral bias in sea surface temperature (SST) that results from assuming a temperature-independent emissivity. The four cases shown correspond to four combinations of atmospheric profile and surface temperature (see legend). The bias is plotted for a view angle of: (a) 0°, and (b) 55°. See text for further details.

7. Conclusions

The effects of salinity on sea surface emissivity are found to be well modelled using the standard refractive index correction of Friedman (1969). However, we find the variation due to dependence on temperature, which has not previously been included in model schemes, to be larger in magnitude than that due to salinity. Particular variation of emissivity around 750–850 cm^{-1} makes this spectral region problematic for SST retrieval without a thorough parametrization of emissivity with temperature. By contrast, the emissivity around 920 cm^{-1} appears to show no significant temperature dependence. A combination of aircraft and ground-based interferometer retrievals has enabled a temperature-dependent refractive index for seawater to be determined that is in broad agreement with existing laboratory data (Pinkley *et al.* 1977). Although subject to some uncertainty due to measurement errors, this refractive index is likely to be more accurate in calculations of emissivity at low temperatures than existing datasets valid at room temperature.

We have analysed the impact of our results on satellite SST retrievals, and find the effect on high-resolution infrared sounders to be significant. Biases in inferred SST approach -0.6 K at 55° for the coldest sea temperatures at some frequencies around 800 cm^{-1}, and may exceed this for larger view angles. It is likely, therefore, that errors in existing emissivity schemes will contribute to latitude-dependent biases which are greatest for large-angle views of cold oceans. There may also be an impact on cloud detection schemes used in high-resolution sounding, which often rely on identification of brightness temperature differences between window channels. Efforts to validate AIRS and IASI radiances at high spectral resolution should benefit from including a temperature-dependent sea surface emissivity.

Acknowledgements

We thank the numerous Met Office staff at the Meteorological Research Flight in Farnborough who helped in the preparation of the ground-based experiments, and Stephan Havemann for useful discussions on sea surface reflection.

REFERENCES

Anderson, G. P., Clough, S. A., Kneizys, F. X., Chetwynd, J. H. and Shettle, E. P. 1986 'AFGL atmospheric constituent profiles (0–120 km)'. Technical Report AFGL-TR-86-0110, Phillips Laboratory, Hanscombe Airforce Base, Mass., USA

Aumann, H. H. and Miller, C. 1995 Atmospheric infrared sounder (AIRS) on the Earth Observing System. *Proc. SPIE, Int. Soc. Opt. Eng.*, **2583,** 332–338

Bertie, J. E. and Lan, Z. 1996 Infrared intensities of liquids XX: The intensity of the OH stretching band of liquid water revisited, and the best current values of the optical constants of H_2O(l) at 25 °C between 15 000 and 1 cm^{-1}. *Appl. Spectrosc.*, **50,** 1047–1057

Cayla, F. and Javelle, P. 1995 IASI instrument overview. *Proc. SPIE, Int. Soc. Opt. Eng.*, **2583,** 271–281

Cox, C. and Munk, W. 1954 Measurements of the roughness of the sea surface from photographs of the sun's glitter. *J. Opt. Soc. Am.*, **44,** 838–850

Downing, H. and Williams, D. 1975 Optical constants of water in the infrared. *J. Geophys. Res.*, **80,** 1656–1661

Edwards, D. P. 1992 'GENLN2: A general line-by-line atmospheric transmittance and radiance model'. NCAR Tech. Note NCAR/TN-367+STR. National Center for Atmospheric Research, Boulder, CO, USA

Fiedler, L. and Bakan, S. 1997 Interferometric measurements of sea surface temperature and emissivity. *German J. Hydrography*, **49,** 357–365

Friedman, D. 1969 Infrared characteristics of ocean water. *Appl. Opt.*, **8,** 2073–2078

Hale, G. M. and Querry, M. R. 1973 Optical constants of water in the 200 nm to 200 μm wavelength region. *Appl. Opt.*, **12,** 555–563

Masuda, K., Takashima, T. and Takayama, Y. 1988 Emissivity of pure and sea waters for the model sea surface in the infrared window regions. *Remote Sensing Environ.*, **24,** 313–329

Merchant, C. J. 2005 'Bias and cloud screening issues in infrared sea surface temperature'. In Proceedings of the fifth GODAE High Resolution SST Pilot Project workshop, Townsville, Australia. International GHRSST-PP Project Office, Hadley Centre for Climate Prediction and Research, Met Office, FitzRoy Road, Exeter, UK

Minnett, P. J., Knuteson, R. O., Best, F. A., Osborne, B. J., Hanafin, J. A. and Brown, O. B. 2001 The marine–atmospheric emitted radiance interferometer: A high-accuracy, seagoing infrared spectroradiometer. *J. Atmos. Oceanic Technol.*, **18,** 994–1013

Pinkley, L. W. and Williams, D. 1976 Optical properties of sea water in the infrared. *J. Opt. Soc. Am.*, **66,** 554–558

Pinkley, L. W., Sethna, P. P. and Williams, D. 1977 Optical constants of water in the infrared: Influence of temperature. *J. Opt. Soc. Am.*, **67,** 494–499

Salisbury, J. W., D'Aria, D. M. and Sabins, F. F. 1993 Thermal infrared remote sensing of crude oil slicks. *Remote Sensing Environ.*, **45,** 225–231

Samuelsson, M. 1996 Interannual salinity variations in the Baltic Sea during the period 1954–90. *Continental Shelf Res.*, **16,** 1463–1477

Sidran, M. 1981 Broadband reflectance and emissivity of specular and rough water surfaces. *Appl. Opt.*, **20,** 3176–3183

Smith, W. L., Knuteson, R. O., Revercomb, H. E., Feltz, W., Howell, H. B., Menzel, W. P., Brown, O., Brown, J., Minnett, P. and McKeown, W. 1996 Observations of the infrared radiative properties of the ocean—Implications for the measurement of sea surface temperature via satellite remote sensing. *Bull. Am. Meteorol. Soc.*, **77,** 41–51

Taylor, J. P., Newman, S. M., Hewison, T. J. and McGrath, A. 2003 Water vapour line and continuum absorption in the thermal infrared—Reconciling models and observations. *Q. J. R. Meteorol. Soc.*, **129,** 2949–2969

Watts, P. D., Allen, M. R. and Nightingale, T. J. 1996 Wind speed effects on sea surface emission and reflection for the Along Track Scanning Radiometer. *J. Atmos. Oceanic Technol.*, **13,** 126–141

Wilson, S. H. S., Atkinson, N. C. and Smith, J. A. 1999 The development of an airborne infrared interferometer for meteorological sounding studies. *J. Atmos. Oceanic Technol.*, **16,** 1912–1927

Wu, X. and Smith, W. L. 1997 Emissivity of a rough sea surface for 8–13 μm: modeling and verification. *Appl. Opt.*, **36,** 2609–2619